



Dynamic recrystallization behavior during hot deformation of as-cast 4Cr5MoSiV1 steel

Yahui Han¹, Changsheng Li^{1,*} , Jinyi Ren¹, Chunlin Qiu¹, Shuaishuai Chen¹, and En Li¹

¹ State Key Lab of Rolling and Automation, Northeastern University, Shenyang 118019, People's Republic of China

Received: 29 July 2020

Accepted: 8 January 2021

Published online:

27 January 2021

© The Author(s), under exclusive licence to Springer Science+Business Media, LLC part of Springer Nature 2021

ABSTRACT

The dynamic recrystallization behavior of as-cast 4Cr5MoSiV1 steel was studied by hot compression tests conducted at various temperatures (900–1150 °C) and strain rates (0.01–10 s⁻¹). Flow stress curves and microstructural observation were employed to experimentally identify the various flow mechanisms during deformation. A revised Sellars' constitutive equation was adopted to construct the thermal activation energy map, which considered the effects of deformation temperature and strain rate on the material variables. The Johnson–Mehl–Avrami–Kolmogorov (JMAK) type equation $X_D = 1 - \exp[-k(\frac{\epsilon - \epsilon_c}{\epsilon_p})^m]$, ($\epsilon \geq \epsilon_c$) was applied to characterize the evolution of dynamic recrystallization (DRX) volume fraction. The nucleation of DRX was performed by the bulging, sub-grain swallowing. The presence of dendrite segregation would affect the DRX to a large extent that the segregated alloying elements and carbide precipitates inhibited the migration of boundaries. The thermal activation energy varied from 4310 to 470 kJ/mol and the thermal activation energy increased sharply at temperature below 1000 °C due to the dendrite segregation. By further analysis of the true stress–strain curves, the material constant m in JMAK type equation was determined to be 1.29366, indicating the DRX was difficult.

Introduction

4Cr5MoSiV1 steel (AISI H13) is famous for its high strength and high stability at high temperature and traditionally used for the hot working die [1]. The industrial products are generally manufactured by the melting-casting, hot forging and a series of heat-

treatments, such as annealing, quenching and tempering. Consequently, the excellent mechanical properties can be obtained if the homogenized and fine microstructure can be controlled. So far, for getting the homogenized and fine microstructure, scholars have done a lot of efforts, such as the adjust of chemical composition [2, 3], the application of powder metallurgy and spray forming [4, 5], the

Handling Editor: Avinash Dongare.

Address correspondence to E-mail: lics@ral.neu.edu.cn

improvement in the hot forging and the heat treatment technology [6–8]. It is widely known that there exist coarse grains and extensive dendrite segregation in as-cast 4Cr5MoSiV1 steel [9]. The coarse microstructure will be broken and the dendrite segregation extended into banding segregation. It is noted that the microstructural heritability of 4Cr5MoSiV1 steel is remarkable, which has been studied by a lot of researchers. Zhou [10] and Grange RA [11] studied the evolution of banding segregation caused by hot forging of dendrite segregation of H13 steel, they reported that the banding segregation would be inherited into quenching and tempering states and affected the homogeneity of quenched and tempered structure of H13 steel directly. Corwyn [12] reported that the heat treatments (anneal-quenching-tempering) cannot significantly improve the uneven distribution of elements and eliminated banding segregation after hot forging. Li [13] studied the influence of forging ratio on the grain structure heredity of H13 steel, it indicated that grain size gradually decreased with the increase of forging ratio, more nucleation points and storage energy were provided for the recovery and recrystallization of grains in the subsequent spheroidizing annealing stage, promoting the grain refinement.

As illustrated above, for a given as-cast 4Cr5MoSiV1 steel, the initial hot forging is an essential and vital factor to improve the final mechanical properties [14, 15]. During forging, dynamic recrystallization is traditionally termed as an efficient method to determine the final microstructure in this class of material [16]. Li [17] studied the dynamic recrystallization (DRX) behavior of H13-mod steel during hot compression in the temperature range of 900–1150 °C and strain rate range of 0.01–10 s⁻¹, the results showed that significant DRX was found at both low and high strain rates. Zhang [18] studied the hot compression deformation behavior of spray-formed H13 steel and cast H13 steel at temperatures of 850–1150 °C, strain rates of 0.1–10 s⁻¹. As a result of the much finer and more homogeneous grain structures of spray-formed H13 steel, the recrystallization behavior was promoted, which was beneficial to the hot deformation. Both the deformation temperature and strain rate had obvious influences on the dynamic recrystallization. Zhao [19] reported that the H13 steel containing rare earth under high strain rate had the discontinuous recrystallization behavior and the stress was elevated obviously, whose thermal activation energy was

573 kJ/mol. The dynamic recrystallization is related to the dislocation slip, whose degree of difficulty is up to the activation energy [20]. The activation energy, which can be derived with the Arrhenius type constitutive equations [21], is generally regarded as an indicator of the difficulty during hot deformation [22]. In addition, based on the Avrami function [23], DRX kinetics models are proposed to describe the fact that the microstructural evolution when the strain surpasses a critical strain, indicating the relationship between DRX volume fraction and process parameters [24]. Therefore, the evolution of DRX can be reflected from activation energy and DRX kinetics model. For example, Wang [22], Peng [25] and Yue [26] et al. showed that the activation energy was sensitive to the thermo-mechanical parameters and cannot be treated as a constant, the DRX may be promoted under deformation conditions with low activation energy. Jin [27] showed that the addition of RE, the introduction of intermetallic compounds and the segregation of Zr element near the grain boundaries contributed to the high activation energy of the Mg-3.7Gd-2.9Y-0.7Zn-0.7Zr magnesium alloy, it indicated that activation energy was also affected by the chemical component, element segregation and phase structure. Zhang [28], Xu [29] and Liu [30] et al. constructed the kinetics models of dynamic recrystallization (DRX) in the form of Avrami function to describe the development of DRX process, and there was a good agreement between the experimental data and the predicted values, which confirmed that the established kinetics of DRX can be applied to model the microstructural evolution.

As point out in [31, 32], particles and segregation could remarkably improve the efficiency of the grain refinement during deformation. Furthermore, the refined grains with more grain boundary area is helpful to accelerate the diffusion process in dendrite segregation region [33]. In as-cast 4Cr5MoSiV1 steel, alloying elements of chromium, molybdenum and vanadium are enriched in the dendrite segregation region and is likely to form the carbide particles during hot deformation. The effect of solute dragging and precipitate pinning in dendrite segregation region on the dynamic recrystallization could be more remarkable than the neighboring matrix. The study on the effect of dendrite segregation on the dynamic recrystallization of as-cast 4Cr5MoSiV1 steel is still absent. Therefore, it is significant to investigate the dynamic recrystallization behavior to guide the

hot forging process. In the present study, the hot compression tests under different conditions were performed, aiming to investigate the microstructural evolution under different deformation conditions. In the meanwhile, the activation energy and the DRX kinetic equation were constructed to predict the DRX evolution.

Experimental procedure

The experimental steel was manufactured by vacuum induction melting (VIM) in a laboratory, whose size of ingot was $\Phi 113 \times 200$ mm. The chemical composition was C 0.40%, Si 0.89%, Mn 0.42%, V 1.01%, Cr 5.15% and Mo 1.74% in weight, the other elements P, S and N each had a concentration of less than 0.02%, and balance Fe. The cylinder specimens of $\Phi 8 \times 15$ mm were machined from the columnar grain zone in the ingot, the original as-cast microstructure with the heterogeneous grain size range of 20–120 μm and dendrite segregation is listed in Fig. 1. The single pass hot compression tests were designed to study the microstructural evolution under different deformation conditions on MMS-200 thermo-mechanical simulator. The entire surface of the cylinder specimen was carefully polished and two tantalum sheets with graphite powder were placed at the end of face, aiming to minimize the effect of friction during hot deformation. The hot deformation process was that the cylinder specimen was first heated to 1200 $^{\circ}\text{C}$ for 300 s at rate of 10 $^{\circ}\text{C}/\text{s}$, after that, it was cooled to a specified deformation temperature ranging from 900 $^{\circ}\text{C}$ to 1150 $^{\circ}\text{C}$, at interval of 50 $^{\circ}\text{C}$. A soaking time of 30 s was needed to eliminate the temperature gradient. Subsequently, the cylinder specimen deformed at strain rates of 0.01 s^{-1} , 0.1 s^{-1} , 1 s^{-1} and 10 s^{-1} . The deformation specimens were immediately quenched to room temperature by water to preserve the high temperature deformation microstructures.

The data obtained by hot compression tests were processed by origin 9.0. The deformation specimens were cut into two identical parts along the direction of hot compression, the section was handled by standard metallographic procedures and then etched with 5% nitric acid for microstructural observation on a BX53MRF OLYMPUS optical microscopy (OM) and a QUANTA 600 scanning electron microscopy (SEM). The fine microstructure was analyzed by a FEI Tecnai

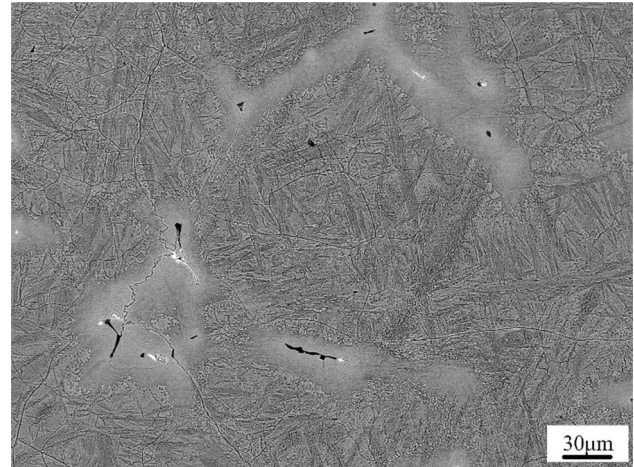


Figure 1 Original as-cast microstructure.

G2 F2 transmission electron microscopy (TEM). Thin foil specimens were prepared by electrochemical polishing at 32 $^{\circ}\text{C}$ for 20 s in a solution containing 10% perchloric acid and 90% methanol.

Result and discussion

Flow stress behavior

The true stress–strain curves in the temperature range of 1000–1150 $^{\circ}\text{C}$ at strain rates of 0.01 s^{-1} , 0.1 s^{-1} and 1 s^{-1} are plotted in Fig. 2. As we can see, the flow stress was concerned with the deformation temperature, strain rate and strain, which increased rapidly at some initial distance and maintained a steady-state level at a large strain. Such behaviors have been shown to be typical for DRX [34]. Moreover, it is noted that the shapes of true stress–strain curves at different strain rates were different. During deformation, with the increase of strain at a certain temperature and strain rate, there always existed the competitive mechanism between the work hardening and softening, the latter is often aroused by the dynamic recovery (DRV) and dynamic recrystallization (DRX) [35]. Figure 3 presents the typical microstructures of as-cast H13 steel specimens deformed at a strain rate of 0.1 s^{-1} and at 1100 $^{\circ}\text{C}$ with true strains of 0.2, 0.4, and 0.6, among which Fig. 3a–b are the optical images and Fig. 3d–f are fine structures based on the TEM observations. It can be seen that there are distinct differences in morphology at different strains. As point out in Fig. 3a and d, the microstructure at a low strain of 0.2 was

characterized by a slightly deformed structure, the prior grain boundaries of austenite were serrated. Additionally, the dislocation density increased and tangled in the grain boundary or at the interface of between particle and matrix, which in turn inhibited the dislocation slip and the stress required for the dislocation slip would increase sharply [36–38]. As the strain increased to 0.4, the microstructure of the deformed specimen contained some recrystallization grains (Fig. 3b). In the distorted regions without recrystallization, the tangled dislocation would form the dislocation cells by the restructuring and combination of dislocation (Fig. 3e) [39, 40]. When the specimen deformed to a strain of 0.6, the number of recrystallization grains increased and partial distorted microstructures evolved into the fine recrystallization grains (Fig. 3c). The typical microstructure was characterized by sub-grains containing a rather low dislocation density (Fig. 3f). By absorbing lattice dislocation, the orientation difference between the

sub-grain boundary and the matrix increased, and the sub-grain boundary became the large-angle grain boundary. When the large-angle grain boundary reached the critical nucleation size, it developed into the recrystallization core [37, 41]. In this period, the magnitude of the strain rate determined the density of tangled dislocation and the rate of dislocation annihilation. It is obvious that, at a lower strain rate, there would be more time for the dislocation annihilation and the work hardening rate was correspondingly small.

By the function $\theta = \frac{\partial \sigma}{\partial \epsilon} |_{T, \dot{\epsilon}}$ [42], the peak stress can be determined. The variation of peak stress at different temperatures and at different strain rates are plotted in Fig. 2d. It can be seen that the peak stress was also related to the deformation conditions, it decreased with the increase of deformation temperature and the decrease of strain rate, indicating that the softening ability increased and thus the DRX was dominant during the subsequent deformation.

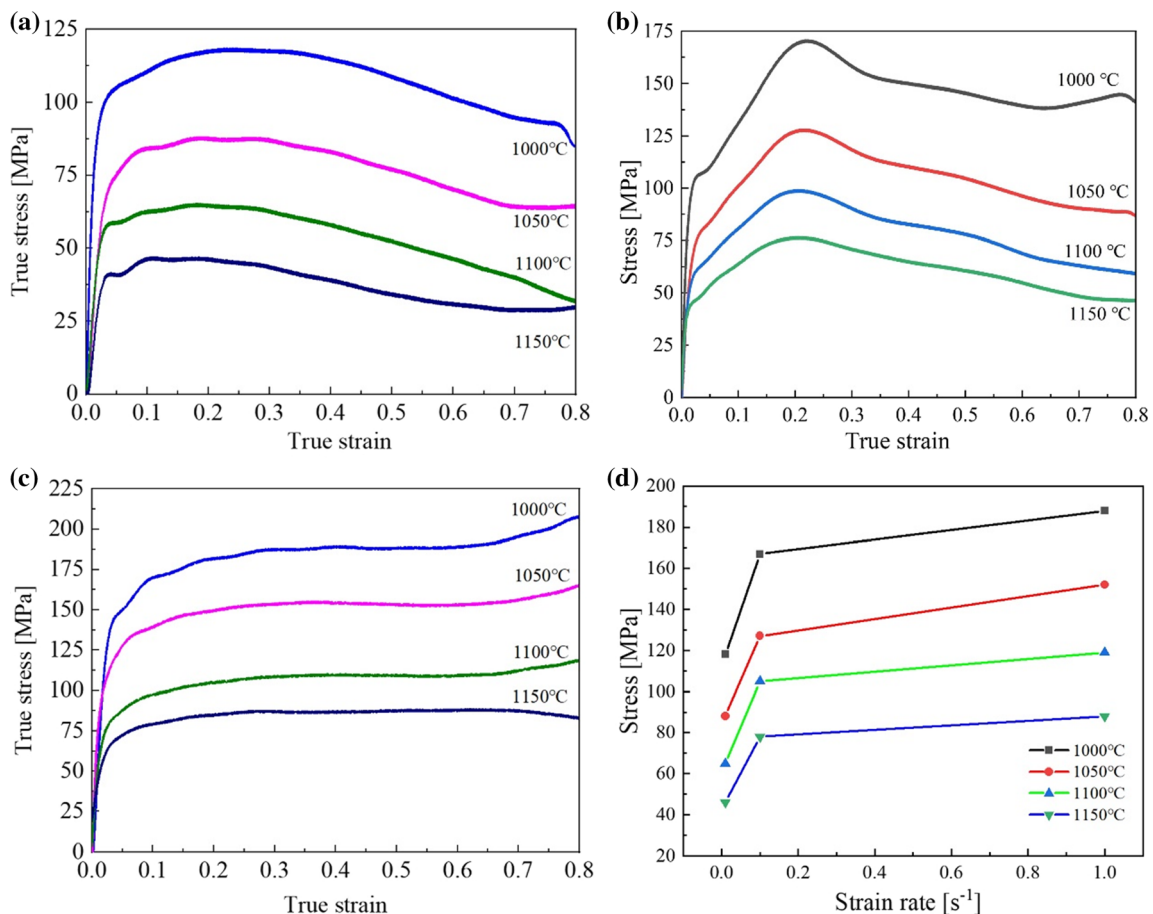


Figure 2 True stress–strain curves of as-cast 4Cr5MoSiV1 steel at different deformation temperature with strain rate: **a** 0.01 s⁻¹; **b** 0.1 s⁻¹; **c** 1 s⁻¹ and **d** Variation of peak stress at 0.01 s⁻¹, 0.1 s⁻¹ and 1 s⁻¹.

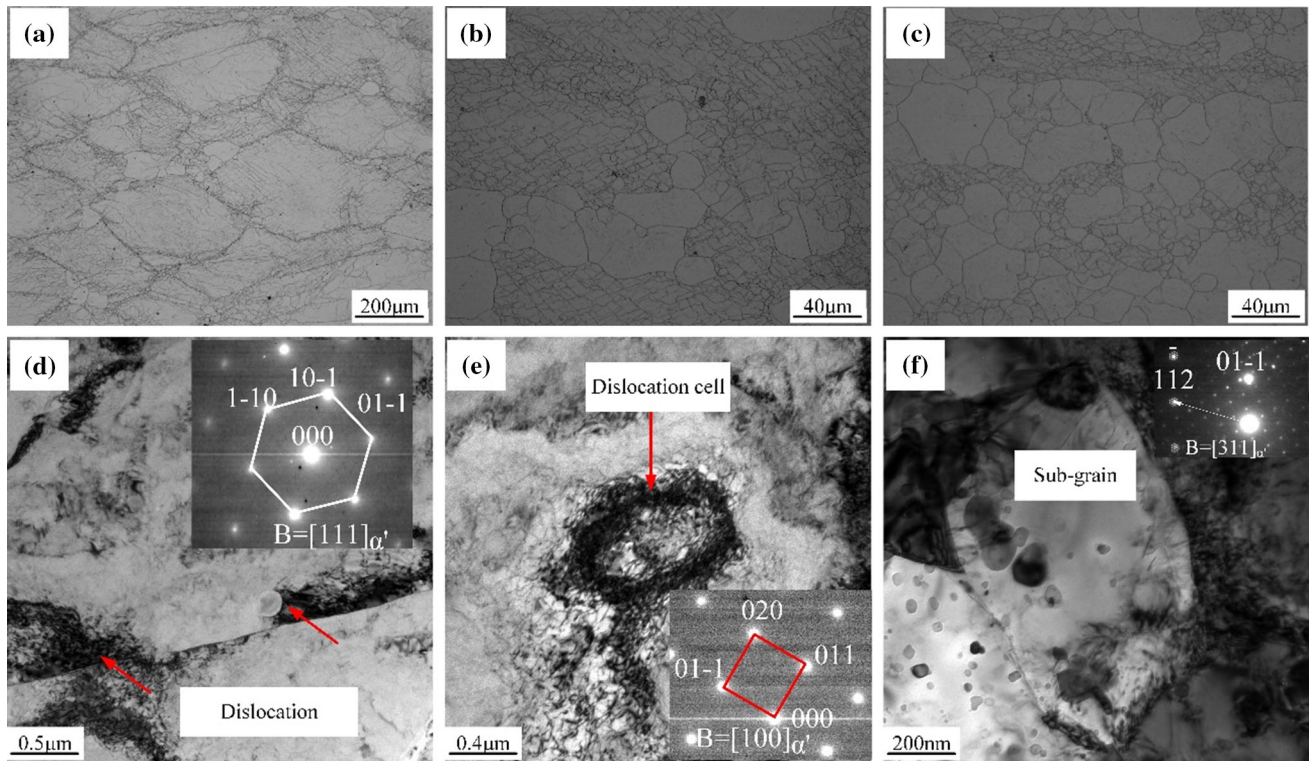


Figure 3 Microstructural changes of as-cast 4Cr5MoSiV1 steel at 1100 °C and 0.1 s^{-1} with various strains: **a, d** $\varepsilon = 0.2$, arrow marks show the dislocation, the inset is a selected area diffraction

pattern (SADP); **b, e** $\varepsilon = 0.4$, arrow marks show the dislocation cell, the inset is a SADP; and **c, f** $\varepsilon = 0.6$, sub-grain, the inset is a SADP.

Recrystallization microstructure observation

Figure 4 illustrates the optical microstructures under different conditions of $1000 \text{ °C} \cdot 1 \text{ s}^{-1}$, $1100 \text{ °C} \cdot 1 \text{ s}^{-1}$, $1150 \text{ °C} \cdot 0.1 \text{ s}^{-1}$ and $1150 \text{ °C} \cdot 0.01 \text{ s}^{-1}$, respectively. In Fig. 4a–d, the microstructures of deformed specimens partially or completely transformed into those of approximately equiaxed grains. With increasing deformation temperature and decreasing strain rate, the deformed microstructure got more homogeneous and the DRX fraction gradually increased. In Fig. 4a, the chain recrystallization structure of the multiple layers and first layer were identified on the original deformed grains, as indicated by red arrows. Besides, partial recrystallization grains grew up. In fact, the dynamic recrystallization behavior of metal materials during hot deformation can be considered as a cyclic and mutually reinforcing process [43]. In the initial stage of dynamic recrystallization, the chain recrystallization grains first form along the original austenite boundary, i.e., the formation of first layer structure. In the meanwhile, the new formed first layer recrystallization grains will also be deformed,

the grain interior will generate a certain proportion of dislocation. The interaction of these dislocations results in the formation of sub-grain boundaries that are connected to large angle grain boundaries. Due to the effect of surface tension, the sub-grain boundary has a drag effect on the large-angle grain boundary, which weakens the migration capacity of the grain boundary. Consequently, nucleation takes place at the original grain boundaries and the nuclei grows toward the local region with the highest stored energy [44]. Stronger adaptivity for grain boundary migration at a higher deformation temperature and sufficient deformation time at a lower strain rate are all helpful to the recrystallization. With the temperature increasing from 1000 to 1100 °C at strain rate of 1 s^{-1} , the deformed microstructure was mostly recrystallized in Fig. 4b, the un-recrystallized regions were surrounded by the recrystallization grains. In Fig. 4c, the partial un-recrystallized regions gradually recrystallized and formed the fine recrystallization grains, whilst the size of the prior recrystallization grains decreased due to the intense dynamic recrystallization effect. In Fig. 4d, there was

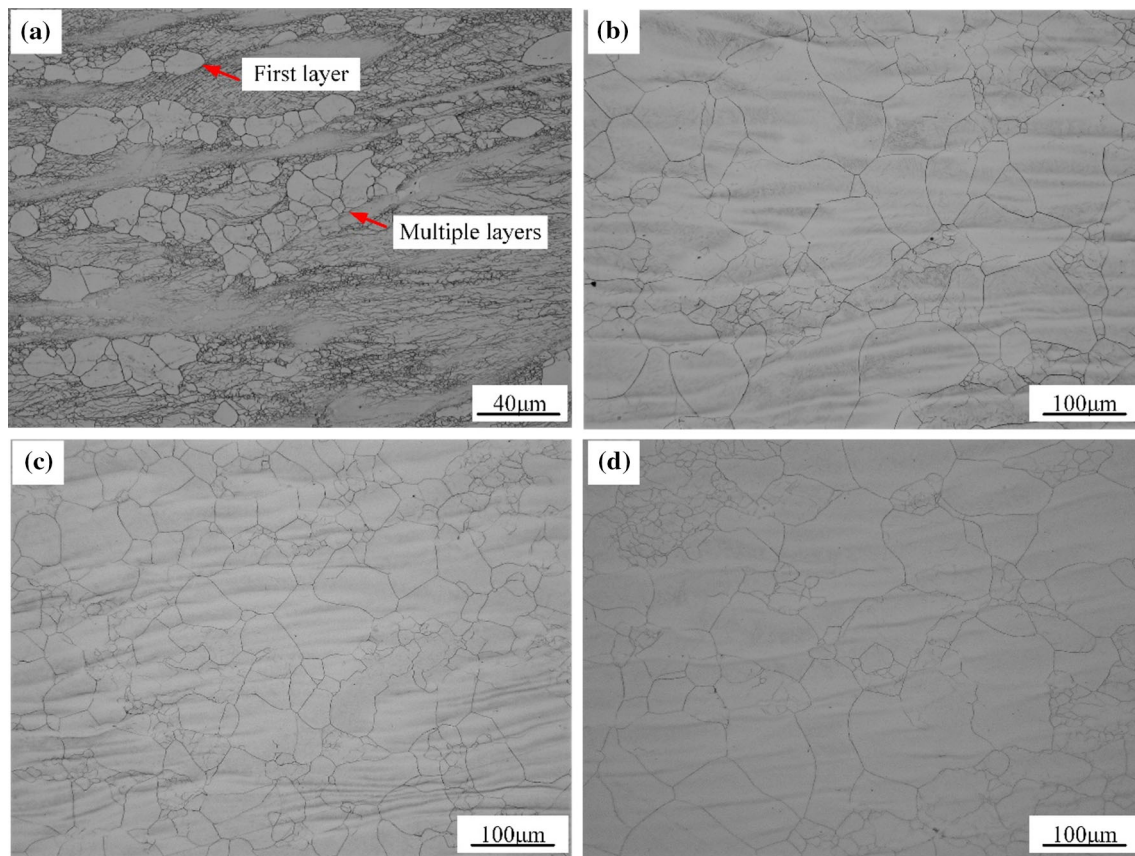


Figure 4 Optical microstructures of as-cast 4Cr5MoSiV1 steel specimens compression tested at different conditions: **a** $1000\text{ }^{\circ}\text{C}^1\text{ s}^{-1}$, arrow marks show the chain recrystallization

structure of the multiple layers and first layer; **b** $1100\text{ }^{\circ}\text{C}^1\text{ s}^{-1}$; **c** $1150\text{ }^{\circ}\text{C}^{0.1}\text{ s}^{-1}$ and **d** $1150\text{ }^{\circ}\text{C}^{0.01}\text{ s}^{-1}$.

more time for the progress of dynamic recrystallization at strain rate of 0.01 s^{-1} , the recrystallization grains got coarsened and the grain size was still heterogeneous.

As illustrated in Fig. 1, there was dendrite segregation in as-cast 4Cr5MoSiV1 steel, which will affect the dynamic recrystallization. Figure 5 lists the optical microstructures under different deformation conditions. The dynamic recrystallization fraction increased with the increase of deformation temperature. The dendrite segregation exhibited banding segregation after hot deformation, which was distinct at temperatures of $1000\text{ }^{\circ}\text{C}$ and $1050\text{ }^{\circ}\text{C}$ in Fig. 5a–b. Nevertheless, the band segregation was gradually alleviated at temperatures of $1100\text{ }^{\circ}\text{C}$ and $1150\text{ }^{\circ}\text{C}$ in Fig. 5c–d. The alleviation of dendrite segregation was related to the alloying element diffusion. The diffusion coefficient was proportional to deformation temperature. The finer microstructure with more grain boundary area was also helpful to accelerate the diffusion process in dendrite segregation region [45].

The alloying elements and precipitates in dendrite segregation region had a significant inhibited effect on recovery and recrystallization due to the inhibition of dislocation movement and grain boundary migration. With increasing deformation temperature from 1000 to $1150\text{ }^{\circ}\text{C}$, it can be seen that the deformed original austenite grains gradually transformed into recrystallization grains and the dynamic recrystallization was obviously inhibited in the banding segregation region. At temperatures of $1000\text{ }^{\circ}\text{C}$ and $1050\text{ }^{\circ}\text{C}$, the dynamic recrystallization was insufficient and there still existed the deformed microstructure in dendrite region after deformation. Therefore, the dendrite segregation was not the main factor on the delay of dynamic recrystallization. When deformed at $1100\text{ }^{\circ}\text{C}$ and $1150\text{ }^{\circ}\text{C}$, the dynamic recrystallization was enhanced, the distorted austenite grains in dendrite region and dendrite segregation region eventually evolved into the equiaxed grains. The dynamic recrystallization in dendrite region was completed and the dendrite

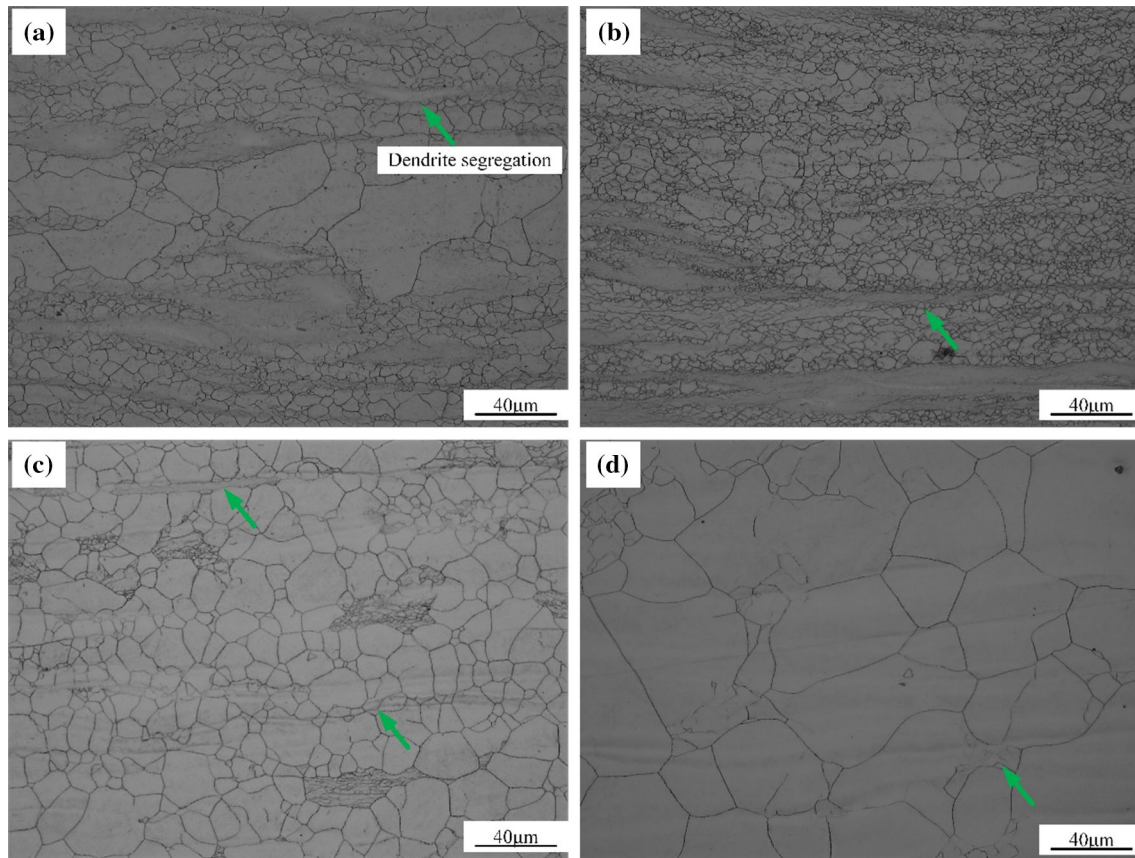


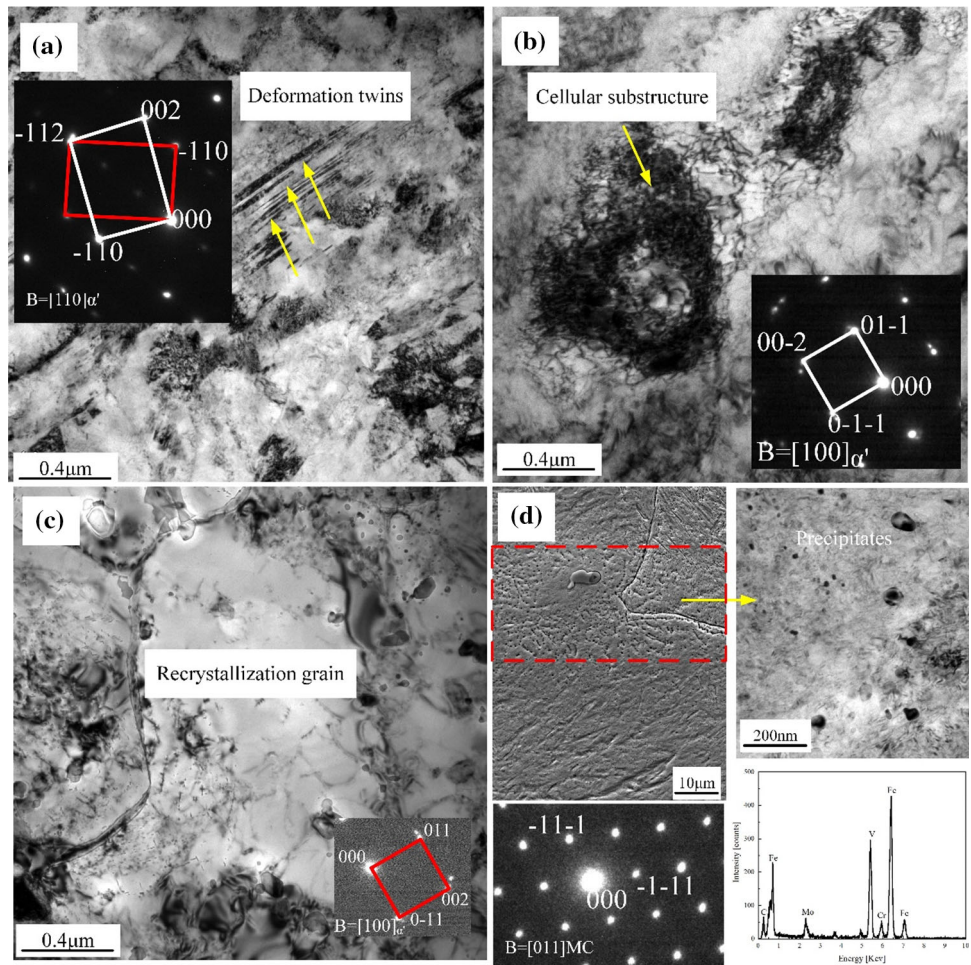
Figure 5 Optical microstructures of as-cast 4Cr5MoSiV1 steel specimens compression tested at different conditions: **a** 1000 °C^{0.01} s⁻¹; **b** 1050 °C^{0.1} s⁻¹; **c** 1100 °C^{0.1} s⁻¹ and **d** 1150 °C¹ s⁻¹. Arrow marks show the dendrite segregation.

segregation became the main factor on the delay of dynamic recrystallization.

In order to further clarify the mechanism of dynamic recrystallization nucleation and growth during hot deformation, the fine microstructures at temperature of 1000 °C and at different strain rates are observed in Fig. 6. At strain rate of 1 s⁻¹ in Fig. 6a, the dislocations in the original austenite would be tangled with each other and had high density. The deformation twins were observed along the < 110 > beam direction, which emerged to release the stress concentration aroused by work hardening [46]. With decreasing strain rate to 0.1 s⁻¹, in Fig. 6b, the deformed microstructure was well improved through the movement and rearrangement of dislocations, the tangled dislocations were gradually developed into the cellular substructure. It was adequate for the progress of dynamic recovery and dynamic recrystallization when the specimen deformed at strain rate of 0.01 s⁻¹. The formed cellular substructure continuously moved to the high-

density dislocation region and engulfed the dislocation. By polygonization, the cellular substructure gradually transformed into a sub-grain with low dislocation density, as indicated in Fig. 6d. This behavior is called the sub-grain swallowing mechanism, which is a continuous dynamic recrystallization behavior [37, 39]. As indicated in Fig. 5, the grain recrystallization was inhibited in the banding segregation region. The alloying elements were enriched in the banding segregation region, the fine secondary precipitates were easy to be generated during hot deformation by the strain-induced mechanism [47]. In Fig. 6d, it can be seen the banding segregation region of deformed microstructure contained abundant fine secondary precipitates. Furthermore, the quantity of secondary precipitates in the matrix not located in the banding segregation region decreased sharply. By TEM observation, the size of precipitates was less than 50 nm, which is thought as effective size that pins austenite grain boundary [48]. EDX analysis further confirmed the nanoscale precipitates

Figure 6 Fine microstructures of as-cast 4Cr5MoSiV1 steel specimens compression tested at 1000 °C and at strain rates of: **a** 1 s⁻¹, arrow marks show the deformation twins and the inset is a selected area diffraction pattern (SADP); **b** 0.1 s⁻¹, arrow marks show the cellular substructure and the inset is a SADP; **c** 0.01 s⁻¹, recrystallization grain in deformed microstructure, the inset is a SADP and **d** 1 s⁻¹, the secondary precipitates in banding segregation region as observed by SEM and TEM, the bottom images are a SADP and EDX analytical result of secondary precipitates.



were vanadium-rich carbides and a selected area diffraction pattern (SADP) demonstrated that the fine precipitates were vanadium carbide (VC).

Thermal activation energy

It is widely acceptable that the thermal activation energy during hot deformation dominates softening mechanism, the value of stored energy will be different under different deformation conditions [22]. Consequently, the recrystallization process and final deformed microstructure will be different accordingly. The activation energy, an important material parameter, determines the critical conditions for DRX initiation. The activation energy of DRX is defined as the energy that must be overcome for the nucleation and growth of new surface or grain boundary [49]. The activation energy is thought to be constant, but in fact it varies with temperature and strain rate. The activation energy Q can be obtained by differentiating the Sellars' constitutive equation:

$$Q = Rn \frac{\partial \{\ln[\sinh(\alpha\sigma)]\}}{\partial(1/T)} = RnS \tag{1}$$

where n is the stress exponent, R is the gas constant and α is a stress state parameter (MPa⁻¹). Among the original solutions in other studies [50], both n and S were always considered to be material constants for simplifications, the mean values of n and S were taken. The effects of deformation temperature and strain rate on the evolution of the activation energy were not considered, the value of activation energy with this approach will be inaccurate.

In our experiment, the values of n (slopes of the $\ln[\sinh(\alpha\sigma_p)] - \ln \dot{\epsilon}$ plots) at each temperature were considerably different, as shown in Fig. 7a. Likewise, the values of S (slopes of $\ln[\sinh(\alpha\sigma_p)] - 10000/T$) at each strain rate were also remarkably different in Fig. 7b. The values of n were dependent on temperature and the values of S were dependent on strain rate. Therefore, the original Sellars' equation cannot

adequately represent the hot deformation behavior of experimental alloys.

A revised Sellars' equation was proposed and applied in many studies [21, 22]:

$$\dot{\epsilon} = A(T, \dot{\epsilon}) [\sinh(\alpha\sigma_p)]^{n(T)} \exp\left(\frac{-Q(T, \dot{\epsilon})}{RT}\right) \quad (2)$$

where n is assumed as a function of temperature and A is a function of both temperature and strain rate.

Taking the natural logarithm on the both sides of Eq. 2,

$$\ln \dot{\epsilon} = \left[\ln QA(T, \dot{\epsilon}) - \frac{Q(T, \dot{\epsilon})}{RT} \right] + n(T) \ln [\sinh(\alpha\sigma_p)] \quad (3)$$

At a certain strain, partial differentiation of Eq. 3 given

$$Q(T, \dot{\epsilon}) = Rn(T) \left[\frac{\partial \ln [\sinh(\alpha\sigma_p)]}{\partial (1/T)} \right]_{\dot{\epsilon}} + P \quad (4)$$

$$P = \left\{ R \ln [\sinh(\alpha\sigma_p)] \left[\frac{\partial n(T)}{\partial (1/T)} \right]_{\dot{\epsilon}} + R \left[\frac{\partial \ln A(T, \dot{\epsilon})}{\partial (1/T)} \right]_{\dot{\epsilon}} - \frac{1}{T} \left[\frac{\partial Q(T, \dot{\epsilon})}{\partial (1/T)} \right]_{\dot{\epsilon}} \right\} \quad (5)$$

The expression P was assumed to be zero [51], and thus Eq. 4 can be simplified as

$$Q(T, \dot{\epsilon}) = Rn(T) \left[\frac{\partial \ln [\sinh(\alpha\sigma_p)]}{\partial (1/T)} \right]_{\dot{\epsilon}} = Rn(T)S(\dot{\epsilon}) \quad (6)$$

Based on the values of n and S obtained in Fig. 7, operations of regression fitting on $T-n$ and $\ln \dot{\epsilon}-S$ were achieved and there were good correlations, as shown in Fig. 8.

$$n = 5.132 + 9.797E11 \exp(0.027T) \quad (7)$$

$$S = 1.338 - 0.1 \ln \dot{\epsilon} + 0.003 \ln \dot{\epsilon}^2$$

By substituting Equations. 7 and 8 into Eq. 6, the activation energy Q can be expressed as a function of deformation temperature T and strain rate $\dot{\epsilon}$.

$$Q = 57.088 - 4.265 \ln \dot{\epsilon} + 0.128 \ln \dot{\epsilon}^2 + B \exp(-0.027T) \quad (9)$$

$$B = 1.09E16 - 8.141E14 \ln \dot{\epsilon} + 2.15E13 \ln \dot{\epsilon}^2 \quad (10)$$

Based on Eq. 1, the calculated Q values from the experimental data were achieved by substituting the values of n at each deformation temperature and S at each strain rate, as shown in Fig. 9a. It can be seen that the experimental Q values varied from 4310 to 470 kJ/mol with a wide range, which tended to decrease with increasing temperature and strain rate, attaining the peak value under the most severe condition (1173 K, 0.01 s⁻¹). Moreover, it can be detected that the Q values were sensitive to deformation conditions and the plastic deformation was easy to proceed as the temperature and strain rate increased. The predicted results of Q values according to

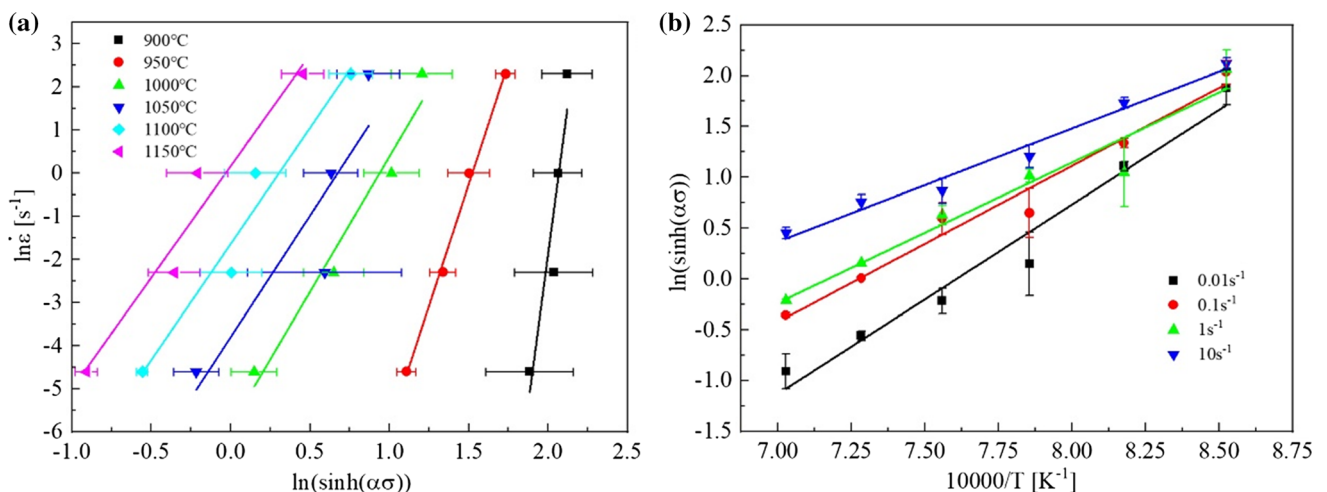


Figure 7 Relationships among flow stress, strain rate and deformation temperature **a** $\ln[\sinh(\alpha\sigma)]$ versus $\ln(\dot{\epsilon})$ and **b** $\ln[\sinh(\alpha\sigma)]$ versus $10000/T$.

Equations 9 and 10 are plotted in Fig. 9b. Similarly, the Q values were also distributed in a wide range and sensitive to the deformation conditions. As is known to all, dislocation movement is the main inner thermodynamic mechanism during plastic deformation, the start of dislocation is affected by the energy barrier and the minimum shear stress [52]. When the energy and shear stress surpass the critical barrier, the dislocation will start to move. On one hand, increasing temperature will improve the thermal motion of the atom, whilst the enhanced dynamic recovery reduces the dislocation density, so that the resistance of the crystal lattice to dislocation motion decreases and thus the minimum shear stress required decreases too. On the other hand, the increase of strain rate means the increase of external force and the dislocation multiplication rate, thus leading an augmented shear stress and dynamic recovery rate to activate the motion of dislocations, the energy required decreases correspondingly. Thirdly, the dislocations are likely to be tangled at high strain rate, inhibiting the dislocation movement. In the meanwhile, there will be no enough time for tangled dislocation polygonization. As a summary, increasing temperature and strain rate is helpful to improve the dislocation motion when the first two factors mentioned above are dominated. It is noted there was a good agreement between the experimental results with the calculated results when the deformation temperature was over 1223 K. At temperature below 1223 K, the experimental Q values in Fig. 9a were larger than predicted Q values in Fig. 9b.

In the dendrite segregation region, the dislocations were easy to be tangled and the motion of dislocations needed more energy to overcome the barrier due to the intense work hardening effect. At temperature below 1223 K, the dynamic recrystallization was weak and alloying element diffusion rate was slow, the effect of dendrite segregation on the dislocation motion was remarkable. That is to say, the difference between experimental Q values and predicted Q values could be mainly attributed to the presence of dendrite segregation in experimental steel.

DRX kinetic model

The typical true stress–strain curves are shown in Fig. 10. Owing to the effect of dislocations and thermal activation energy, it can be divided into two types: (a) work-hardening and DRV, (b) work-hardening, DRV and DRX. Work-hardening was throughout the whole deformation process, the variation of true stress was the result of the competition between work-hardening and softening. As can be seen in the uppermost A curve, the value of flow stress σ_r gradually increased and approached the steady state stress. At saturation, the value of asymptotic stress was given by σ_{sat} [42]. DRX appeared when the strain surpassed the value of critical strain (ϵ_c) in the B curve. The work-hardening rate equaled to the softening rate at the peak strain (ϵ_p). The flow stress decreased in the subsequent DRX process, which was defined as σ_{drx} . There was also a

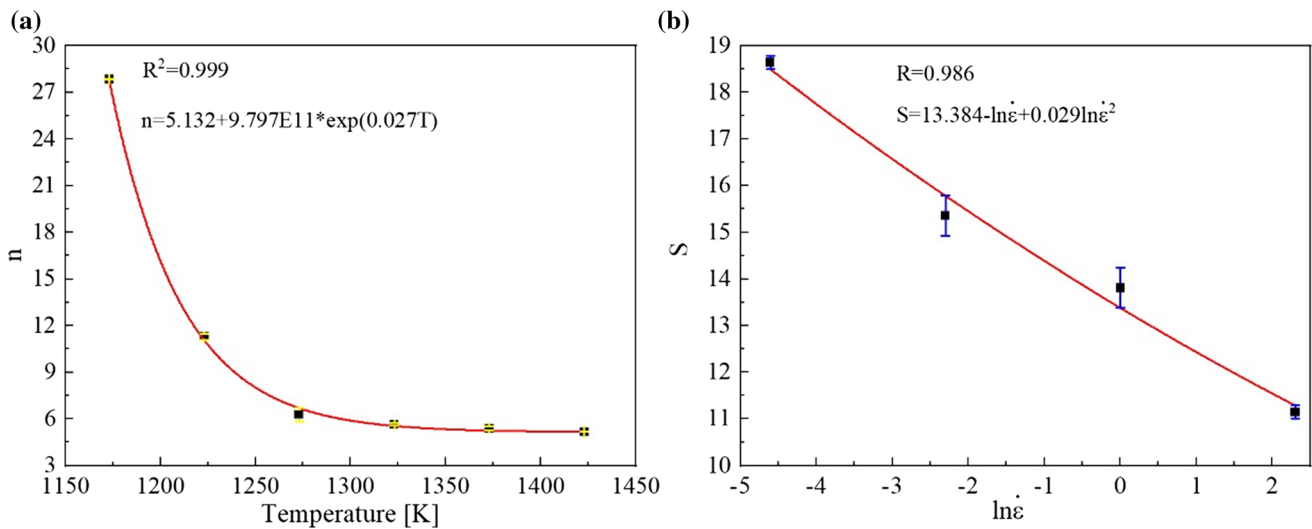


Figure 8 Relationships between a n and T and b S and $\dot{\epsilon}$.

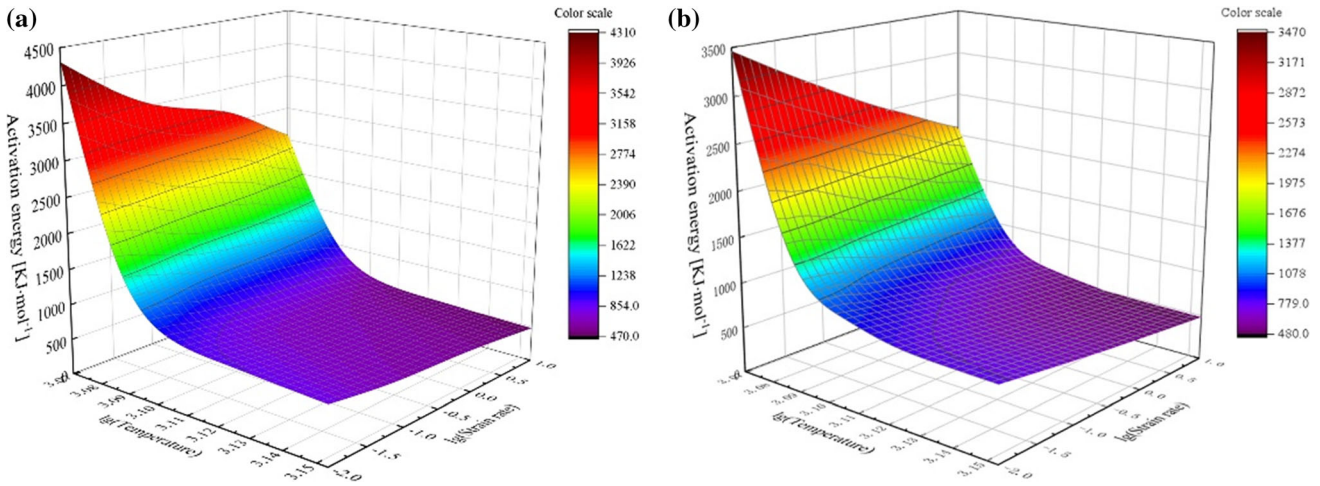


Figure 9 Evolution of Q value (kJ/mol) as a function of deformation temperature and strain rate: **a** experimental results and **b** predicted results.

definition of asymptotic stress σ_{ss} to indicate the level of steady state stress by DRX [29].

As indicated by previous study [30], the volume fraction of DRX (X_D) under given deformation condition can be expressed:

$$X_D = \frac{\Delta\sigma}{\sigma_{max}} = \frac{\sigma_p - \sigma_{drx}}{\sigma_{sat} - \sigma_{ss}} \quad (11)$$

The X_D at a certain strain can be obtained if the parameters σ_{sat} and σ_{ss} under different deformation conditions in Eq. 11 are determined. As an example, the plot of the strain hardening rate (θ) versus flow stress (σ) at a temperature of 1150 °C and at a strain rate of 0.01 s⁻¹ is shown in Fig. 11. From the diagram it can easily determine the peak stress σ_p for DRX and

steady state stress σ_{ss} for complete DRX corresponding to the intersection points between the $\theta - \sigma$ curve and horizontal line. The recrystallization volume fraction X_D would keep increasing until that the flow stress decreased from σ_p to σ_{drx} . The tangent line was made through the critical strain point on the plot to intercept horizontal line at σ_{sat} . The critical strain ϵ_c can be determined by the second numerical derivative of the flow stress σ in true stress–strain curves as a function of $-\partial(\frac{\partial\sigma}{\partial\epsilon})/\partial\sigma$ versus $\sigma|_{T,\dot{\epsilon}}$. The σ_{sat} , σ_{ss} at temperatures of 1000 °C, 1050 °C, 1100 °C and 1150 °C, and at strain rates of 0.01 s⁻¹, 0.1 s⁻¹ and 1 s⁻¹ are listed in Table 1.

Following linear regression, it can be seen that the $\ln \sigma_{sat}$, $\ln \sigma_{ss}$ exhibited reasonably good fit ($R^2_{\ln \sigma_{sat}} = 0.92$, $R^2_{\ln \sigma_{ss}} = 0.82$) with $\ln Z$ ($Z = \dot{\epsilon} \exp(\frac{Q}{RT})$) in Fig. 12a, the following relationship could be observed:

$$\ln \sigma_{sat} = -2.48843 + 0.16875 \ln Z \quad (12)$$

$$\ln \sigma_{ss} = -4.32753 + 0.2003 \ln Z \quad (13)$$

Rearranging Equations. 12 and 13 yields,

$$\sigma_{sat} = 0.08Z^{0.16875} \quad (14)$$

$$\sigma_{ss} = 0.01Z^{0.2003} \quad (15)$$

Meantime, linear aggression was also implemented to deduce the relationship between σ_{sat} and σ_{ss} in Fig. 12b, the expression was attained:

$$\sigma_{ss} = 0.70856\sigma_{sat} - 8.3408 \quad (16)$$

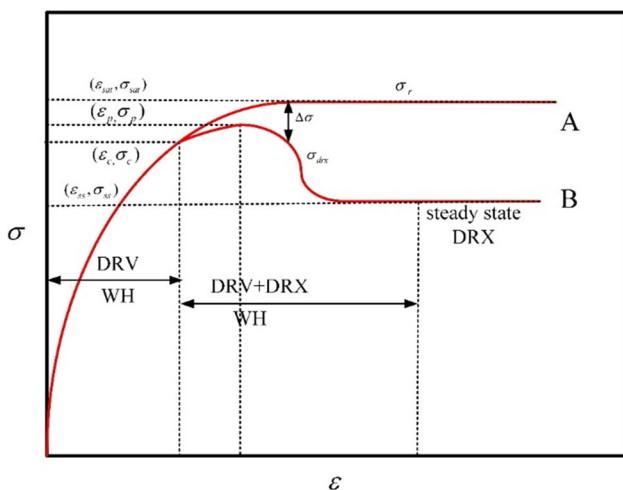


Figure 10 Schematic diagram of the true stress–strain curve for DRX and DRV.

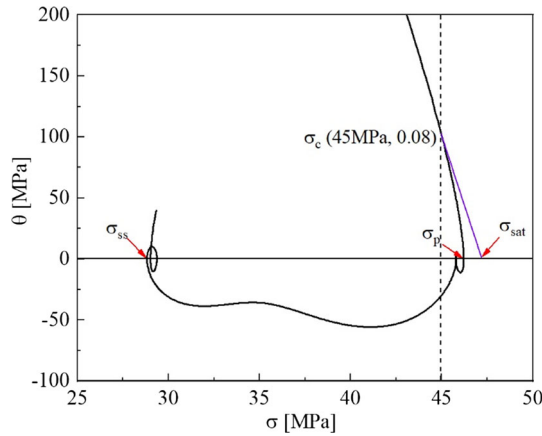


Figure 11 $\theta - \sigma$ curves at a temperature of 1150 °C and a strain rate of 0.01 s⁻¹.

During deformation of metals, part of the deformation energy is used for grain nucleation and growth. The dynamic recrystallization volume fraction X_D in a certain time range can be influenced by the deformed conditions and the generated dislocation substructure. A classical analytical model to describe such a complex process was proposed by Johnson, Mehl, Avrami and Kolmogorov (JMAK) [53], the recrystallization fraction X_D was given by [54]:

$$X_D = 1 - \exp\left(-k\left(\frac{\varepsilon - \varepsilon_c}{\varepsilon_p}\right)^m\right), (\varepsilon \geq \varepsilon_c) \quad (17)$$

where ε is true strain, ε_c is critical strain, ε_p is peak strain. k and m are constants.

By taking natural logarithm on both sides of Eq. 17, it leads to

$$\ln[-\ln(1 - X_D)] = \ln k + m \ln\left(\frac{\varepsilon - \varepsilon_c}{\varepsilon_p}\right) \quad (18)$$

Thus, $m = \frac{\partial \ln[-\ln(1 - X_D)]}{\partial \ln[(\varepsilon - \varepsilon_c)/\varepsilon_p]}$, and the value of $\ln k$ is the intercept on the vertical coordinate. In order to construct the DRX kinetic model, it is necessary to calculate the value of m and k . The values of X_D under different deformation conditions can be determined

Table 1 Values of σ_{sat} and σ_{ss} under different conditions

σ_{sat}/σ_{ss} MPa	1000 °C	1050 °C	1100 °C	1150 °C
0.01 s ⁻¹	141/115	103/63	73/26	47/29
0.1 s ⁻¹	197/160	185/152	124/100	85/68
1 s ⁻¹	247/201	207/165	153/122	98/81

by Eq. 11. By substituting the values of peak strain ε_p and critical strain ε_c into Eq. 18, associating with the dynamic recrystallization fraction X_D at strain of 0.5, 0.6, 0.7 and 0.8 under different deformation conditions, the fitted line is depicted in Fig. 13, the values of k and m were obtained as 0.2595 and 1.29366. Hence, the DRX volume fraction can be expressed as the following equation:

$$X_D = 1 - \exp\left[-0.25949\left(\frac{\varepsilon - \varepsilon_c}{\varepsilon_p}\right)^{1.29366}\right], (\varepsilon \geq \varepsilon_c) \quad (19)$$

Some authors [24, 55, 56] have also described the DRX kinetic model of metals during hot deformation in the form of Eq. 17. In general, the value of time exponent m is in the vicinity of 2. However, the m is also considered to be related to the value of Z-parameter, which surely decreases with increasing Z. The m value 1.29366 in this study was in the vicinity of 1.4 at high Z [57], indicating the DRX of experimental steel was difficult.

Since the parameters of the equation for DRX period have been obtained in above sections, then the flow stress in DRX period can be expressed

$$\sigma = \sigma_p - (\sigma_{sat} - \sigma_{ss}) \left\{ 1 - \exp\left[-0.25949\left(\frac{\varepsilon - \varepsilon_c}{\varepsilon_p}\right)^{1.29366}\right] \right\}, (\varepsilon \geq \varepsilon_c) \quad (20)$$

In order to verify the constitutive equation developed for 4Cr5MoSiV1 hot-working steel in DRX period, as an example, the calculated data from the model and the experimental ones at strain rate 0.01 s⁻¹ and at temperatures of 1000 °C, 1050 °C, 1100 °C and 1150 °C are plotted in a figure, as shown in Fig. 14a. It can be detected that there was a good agreement between the calculated data and the experimental data. Meanwhile, it is widely accepted that the effects of deformation temperature and strain rate on the DRX can be reasonable by the Z-parameter [58]. The combined effects are illustrated in Fig. 14b in the form of contour map in the temperature range of 900–1150 °C and strain rate range of 0.01–10 s⁻¹, contour numbers indicated the value of $\ln Z$ at strain of 0.8 and the tendency of DRX was inversely proportional to the contour numbers. It is noteworthy that the contour number reached the peak at 900 °C and 10 s⁻¹ and attained the minimum value at 1150 °C and 0.01 s⁻¹.

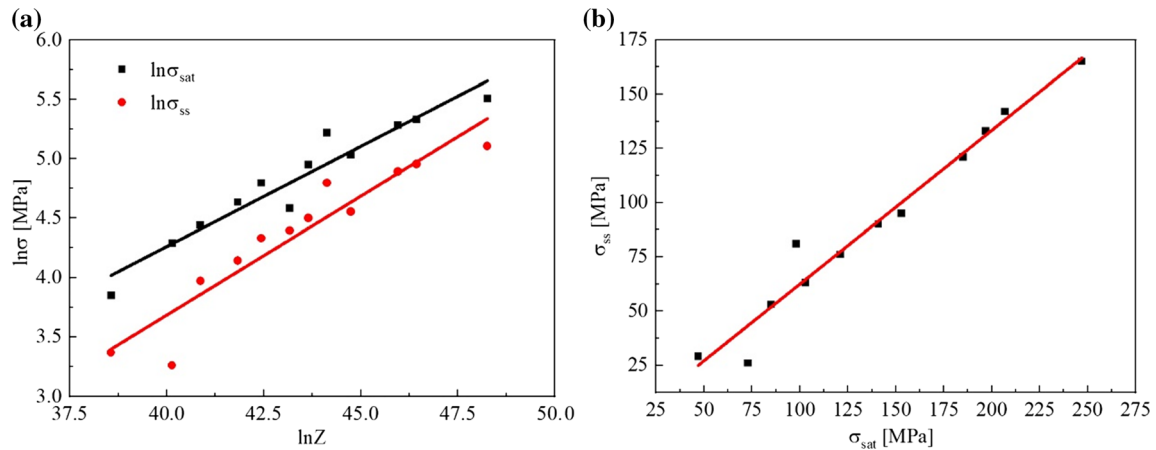


Figure 12 Relationship **a** between $\ln Z$ and $\ln \sigma_{sat}$, $\ln \sigma_{ss}$, and **b** between σ_{sat} and σ_{ss} .

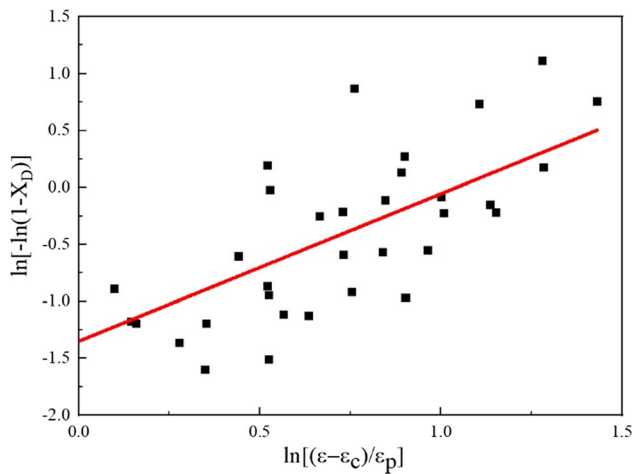


Figure 13 Relationship between $\ln[(\epsilon - \epsilon_c)/\epsilon_p]$ and $\ln[-\ln(1 - X_D)]$.

Conclusion

The dynamic recrystallization behavior of as-cast 4Cr5MoSiV1 steel was studied using isothermal compression tests. Based on the observations and results of this investigation, the following were apparent:

1. The true stress–strain curves presented the typical dynamic recrystallization (DRX) in the temperature range of 1000–1150 °C and strain rate range of 0.01 s⁻¹–1 s⁻¹. The flow stress and peak stress decreased with the increase of deformation temperature and the decrease of strain rate.
2. The DRX fraction increased with increasing deformation temperature and decreasing strain rate. The nucleation of DRX was performed by

the bulging and sub-grain swallowing. The segregated alloying elements and fine precipitates in dendrite segregation region in 4Cr5MoSiV1 steel will inhibit the dislocation motion and grain boundary migration.

3. A revised Sellars' constitutive equation was employed to deduce the expression of thermal activation energy depending on the deformation temperature and strain rate.

$$Q = 57.088 - 4.265 \ln \dot{\epsilon} + 0.128 \ln \dot{\epsilon}^2 + B \exp(-0.027T)$$

$$B = 1.09E16 - 8.141E14 \ln \dot{\epsilon} + 2.15E13 \ln \dot{\epsilon}^2$$

The thermal activation energy maps were constructed, whose values varied from 4310 to 470 kJ/mol. The calculated results agreed well with the experimental results at temperature over 1000 °C. The more thermal activation energy was required at temperature of below 1000 °C due to the dendrite segregation.

4. The Johnson–Mehl–Avrami–Kolmogorov (JMAK) type DRX kinetic equation was determined $X_D = 1 - \exp[-0.25949(\frac{\epsilon - \epsilon_c}{\epsilon_p})^{1.29366}]$, ($\epsilon \geq \epsilon_c$), the m value of 1.29366 meant the DRX was difficult. The stress predicted by the determined JMAK type kinetic equation was coincident with the experimental stress.

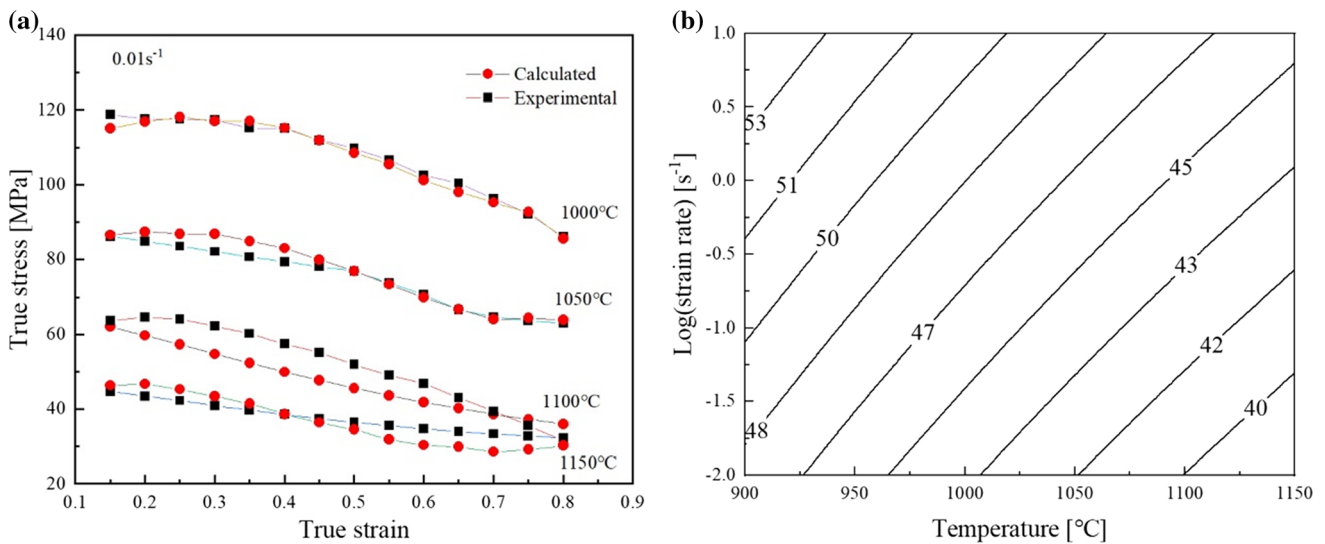


Figure 14 **a** Comparison of the predicted stress by the model with the experimental stress and **b** Z-parameter map at the strain of 0.8.

Acknowledgements

This work was supported by the National Key Research Project of China (2016YFB0300402).

Compliance with ethical standards

Conflict of interest The authors declare that they have no conflict of interest.

References

- Mao M, Guo H, Wang F, Sun X (2019) Effect of cooling rate on the solidification microstructure and characteristics of primary carbides in H13 steel. *ISIJ Int* 59:848–857. <https://doi.org/10.2355/isijinternational.isijint-2018-524>
- Kheirandish S, Noorian A (2008) Effect of Niobium on microstructure of cast AISI H13 hot work tool steel. *J Iron Steel Res* 15:61–66. [https://doi.org/10.1016/S1006-706X\(08\)60145-4](https://doi.org/10.1016/S1006-706X(08)60145-4)
- Wang M, Ma D, Liu Z, Zhou J, Chi H, Dai J (2014) Effect of Nb on segregation, primary carbides and toughness of H13 steel. *Acta Metall Sin* 50:285–293. <https://doi.org/10.3724/SP.J.1037.2013.00490>
- Zhang J, Huang J, Wang H, Lu L, Cui H (2014) Microstructures and mechanical properties of spray formed H13 tool steel. *Acta Metall Sin* 50:787–794. <https://doi.org/10.3724/SP.J.1037.2013.00820>
- Zhang B, Yang F, Qin Q, Lu T, Sun H, Lin S, Chen C, Guo Z (2020) Characterisation of powder metallurgy H13 steels prepared from water atomised powders. *Powder Metall* 63:9–18. <https://doi.org/10.1080/00325899.2019.1692169>
- Pei Y, Ma D, Liu B, Chen Z, Zhou R, Zhou J (2012) Effect of forging ratio on microstructure and mechanical property of H13 steel. *Iron Steel* 47:81–86. <https://doi.org/10.1007/s11783-011-0280-z>
- Wang J, Xu Z, Lu X (2020) Effect of the quenching and tempering temperatures on the microstructure and mechanical properties of H13 Steel. *J Mater Eng and Perform* 29:1849–1859. <https://doi.org/10.1007/s11665-020-04686-0>
- Perez M, Belzunce FJ (2015) The effect of deep cryogenic treatments on the mechanical properties of an AISI H13 steel. *Mater Sci Eng A* 624:32–40. <https://doi.org/10.1016/j.msea.2014.11.051>
- Han Y, Li C, Ren J, Qiu C, Zhang Y, Wang J (2019) Dendrite segregation changes in high temperature homogenization process of as-cast H13 steel. *ISIJ Int* 59:1893–1900. <https://doi.org/10.2355/isijinternational.ISIJINT-2019-148>
- Zhou J, Ma D, Liu B, Kang A, Li X (2012) Research of band segregation evolution of H13 steel. *J Iron Steel Res* 24:47–52. <https://doi.org/10.1007/s11783-011-0280-z>
- Grange RA (1971) Effect of microstructural banding in steel. *Metall Mater Trans B* 2:417–426. <https://doi.org/10.1007/BF02663328>
- Berger CM, Finn J (1995) The effect of annealed microstructure on the impact toughness of premium H13 die steel, Transactions of the 18th international die casting congress and exposition, pp 357–359
- Li C, Zhang Q, Wang P (2017) Influence of forging ratio on heredity rules of grain structure for die steel H13. *Forg Stamp Tech* 42:9–12
- Wang Y, Liu C, Jiang F, Zheng YX, Duan LZ (2015) Influence of forging process on the structure and impact property of electro remelted H13 steel. *Hebei Metall* 6:5–7

- [15] Zhou J, Ma D, Pei Y, Li Z, Liu B, Feng S (2013) Influence of Forging ratio on microstructure and impact property of H13 hot work die steel by electrosmelting. *Mater Mech Eng* 37:73–78
- [16] Huang K, Logé RE (2016) A review of dynamic recrystallization phenomena in metallic materials. *Mater Des* 111:548–574. <https://doi.org/10.1016/j.matdes.2016.09.012>
- [17] Li C, Tan Y, Zhao F (2020) Dynamic recrystallization behaviour of H13-mod steel. *J Iron Steel Res Int* 27:1073–1086. <https://doi.org/10.1007/s42243-020-00462-5>
- [18] Zhang J, Huang J, Cui H, Zhang J (2014) High-temperature thermal deformation and microstructure evolution of spray formed H13 tool steel. *Hot Working Tech* 43:1–5
- [19] Zhao Z, Sun M, Sun J (2017) study on hot deformation behavior and hot processing map of H13 steel containing rare earth. *Mater Rev* 31:149–155
- [20] Esteban-Manzanares G, Santos-Güemes R, Papadimitriou I, Martínez E, LLorca J (2020) Influence of the stress state on the cross-slip free energy barrier in Al: an atomistic investigation. *Acta Mater* 184:109–119. <https://doi.org/10.1016/j.actamat.2019.10.055>
- [21] Shi C, Mao W, Chen X (2013) Evolution of activation energy during hot deformation of AA7150 aluminum alloy. *Mater Sci Eng A* 517:83–91. <https://doi.org/10.1016/j.msea.2013.01.080>
- [22] Wang S, Hou L, Luo J, Zhang J, Zhuang L (2015) Characterization of hot workability in AA 7050 aluminum alloy using activation energy and 3-D processing map. *J Mater Process Tech* 225:110–121. <https://doi.org/10.1016/j.jmatprotec.2015.05.018>
- [23] Irani M, Lim S, Joun M (2019) Experimental and numerical study on the temperature sensitivity of the dynamic recrystallization activation energy and strain rate exponent in the JMAK model. *J Mater Res Technol* 8:1616–1627. <https://doi.org/10.1016/j.jmrt.2018.11.007>
- [24] Quan G, Mao A, Luo G, Liang J, Wu D, Zhou J (2013) Constitutive modeling for the dynamic recrystallization kinetics of as-extruded 3Cr20Ni10W2 heat-resistant alloy based on stress-strain data. *Mater Des* 52:98–107. <https://doi.org/10.1016/j.matdes.2013.05.030>
- [25] Peng X, Su W, Xiao D, Xu G (2018) Investigation on hot workability of homogenized Al-Zn-Mg-Cu alloy based on activation energy and processing map. *JOM* 70:993–999. <https://doi.org/10.1007/s11837-017-2708-9>
- [26] Yue C, Zhang L, Liao S, Pei J, Gao H, Jia Y, Lian X (2009) Research on the dynamic recrystallization behavior of GCr15 steel. *Mater Sci Eng A* 499:177–181. <https://doi.org/10.1016/j.msea.2007.11.123>
- [27] Jin X, Xu W, Shan D, Liu C, Zhang Q (2017) Deformation behavior microstructure evolution and hot workability of Mg-3.7Gd-2.9Y-0.7Zn-0.7Zr alloy. *Met Mater Int* 23:434–443. <https://doi.org/10.1007/s12540-017-6352-2>
- [28] Zhang C, Zhang L, Xu Q, Xia Y, Shen W (2016) The kinetics and cellular automaton modeling of dynamic recrystallization behavior of a medium carbon Cr-Ni-Mo alloyed steel in hot working process. *Mater Sci Eng A* 678:33–43. <https://doi.org/10.1016/j.msea.2016.09.056>
- [29] Xu Y, Tang D, Song Y, Pan X (2012) Dynamic recrystallization kinetics model of X70 pipeline steel. *Mater Des* 39:168–174. <https://doi.org/10.1016/j.matdes.2012.02.034>
- [30] Liu J, Cui Z, Ruan L (2011) A new kinetics model of dynamic recrystallization for magnesium alloy AZ31B. *Mater Sci Eng A* 529:300–310. <https://doi.org/10.1016/j.msea.2011.09.032>
- [31] Jin S, Tao N, Marthinsen K, Li Y (2015) Deformation of an Al-7Mg alloy with extensive structural micro-segregations during dynamic plastic deformation. *Mater Sci Eng A* 628:160–167. <https://doi.org/10.1016/j.msea.2015.01.057>
- [32] Wang J, Hodgson PD, Bikmukhametov L, Miller MK, Timokhina I (2017) Effects of hot-deformation on grain boundary precipitation and segregation in Ti-Mo microalloyed steels. *Mater Des* 141:8–56. <https://doi.org/10.1016/j.matdes.2017.12.023>
- [33] Chen K, Yang Y, Shao G, Liu K (2011) Enhancing the homogenized diffusion of chromium in alloy steel ingot by forging. *Steel Res Int* 82:1325–1331. <https://doi.org/10.1002/srin.201100128>
- [34] Zhang M, Li F, Wang S, Liu C (2010) Characterization of hot deformation behavior of a P/M nickel-base superalloy using processing map and activation energy. *Mater Sci Eng A* 527:6771–6779. <https://doi.org/10.1016/j.msea.2010.07.039>
- [35] Hu H, Zhen L, Zhang B, Yang L, Chen J (2008) Microstructure characterization of 7050 aluminum alloy during dynamic recrystallization and dynamic recovery. *Mater Charact* 59:1185–1189. <https://doi.org/10.1016/j.matchar.2007.09.010>
- [36] Hussein AM, Rao SI, Uchic MD, Dimiduk DM, El-Awady JA (2015) Microstructurally based cross-slip mechanisms and their effects on dislocation microstructure evolution in fcc crystals. *Acta Mater* 85:180–190. <https://doi.org/10.1016/j.actamat.2014.10.067>
- [37] Alizadeh R, Mahmudi R, Ngan AHW, Langdon TG (2017) Microstructural evolution during hot shear deformation of an extruded fine-grained Mg-Gd-Y-Zr alloy. *J Mater Sci* 52(13):7843–7857. <https://doi.org/10.1007/s10853-017-1031-8>
- [38] Samaee V, Sandfeld S, Idrissi H, Groten J, Pardoën T, Schwaiger R, Schryvers D (2020) Dislocation structures and the role of grain boundaries in cyclically deformed Ni

- micropillars. *Mater Sci Eng A* 769:138295. <https://doi.org/10.1016/j.msea.2019.138295>
- [39] Yan L, Shen J, Li Z, Li J, Yan X (2010) Microstructure evolution of Al-Zn-Mg-Cu-Zr alloy during hot deformation. *Rare Met* 29:426–432. <https://doi.org/10.1007/s12598-010-0143-y>
- [40] He B, Hu B, Yen H, Cheng G, Wang Z, Luo H, Huang M (2017) High dislocation density-induced large ductility in deformed and partitioned steels. *Science* 357:1029–1032. <https://doi.org/10.1126/science.aan0177>
- [41] Ma B, Li C, Song Y, Wang J, Sui F (2017) Deformation and recrystallization microtextures of an austenitic steel during asymmetrical hot rolling process. *J Mater Sci* 52(22):13212–13226. <https://doi.org/10.1007/s10853-017-1172-9>
- [42] Zhou P, Ma Q (2017) Dynamic recrystallization behavior and processing map development of 25CrMo4 mirror plate steel during hot deformation. *Acta Metall Sin (Engl Lett)* 30:907–920. <https://doi.org/10.1007/s40195-017-0613-4>
- [43] Mirzadeh H, Najafizadeh A (2012) Modeling and prediction of hot deformation flow curves[J]. *Metall Mater Trans A* 43:108–123. <https://doi.org/10.1007/s11661-011-0836-3>
- [44] Wang S, Zhang M, Wu H, Yang B (2016) Study on the dynamic recrystallization model and mechanism of nuclear grade 316LN austenitic stainless steel. *Mater Charact* 118:92–101. <https://doi.org/10.1016/j.matchar.2016.05.015>
- [45] Chen K, Yang Y, Shao G, Liu K (2011) Effect of recrystallization grain boundary on homogenized diffusion of chromium in alloy steel ingot. *Trans Mater Heat Treat* 32:79–83. <https://doi.org/10.13289/j.issn.1009-6264.2011.05.016>
- [46] Sun B, Fazeli F, Scott C, Brodusch N, Gauvin R, Yue S (2018) The influence of silicon additions on the deformation behavior of austenite-ferrite duplex medium manganese steels. *Acta Mater* 148:249–262. <https://doi.org/10.1016/j.actamat.2018.02.005>
- [47] Hong S, Kang K, Park CG (2002) Strain-induced precipitation of NbC in Nb and Nb-Ti microalloyed HSLA steels. *Scripta Mater* 46:163–168
- [48] Sha Q, Sun Z (2009) Grain growth behavior of coarse-grained austenite in a Nb-V-Ti microalloyed steel. *Mater Sci Eng A* 523:77–84. <https://doi.org/10.1016/j.msea.2009.05.037>
- [49] Xia Y, Liu Y, Mao Y, Quan G, Zhou J (2012) Determination of critical parameters for dynamic recrystallization in Ti–6Al–2Zr–1Mo–1V alloy. *T Nonferr Metal Soc* 22:668–672. [https://doi.org/10.1016/S1003-6326\(12\)61783-X](https://doi.org/10.1016/S1003-6326(12)61783-X)
- [50] Yin F, Hua L, Mao H, Han X (2013) Constitutive modeling for flow behavior of GCr15 steel under hot compression experiments. *Mater Des* 43:393–401. <https://doi.org/10.1016/j.matdes.2012.07.009>
- [51] Huang X, Zhang H, Han Y, Wu W, Chen J (2010) Hot deformation behavior of 2026 aluminum alloy during compression at elevated temperature. *Mater Sci Eng A* 527:485–490. <https://doi.org/10.1016/j.msea.2009.09.042>
- [52] Honeycombe RWK (1984) The plastic deformation of metals, 2nd edn. Edward Arnold Ltd., Maryland
- [53] Radhakrishnan B, Sarma GB, Zacharia T (1998) Modeling the kinetics and microstructural evolution during static recrystallization-Monte Carlo simulation of recrystallization. *Acta Mater* 46:4415–4433. [https://doi.org/10.1016/S1359-6454\(98\)00077-9](https://doi.org/10.1016/S1359-6454(98)00077-9)
- [54] Avrami M (1940) Kinetics of phase change II: transformation-time relations for random distribution of nuclei. *J Chem Phys* 8:212–224. <https://doi.org/10.1063/1.1750631>
- [55] Gu S, Zhang L, Zhang C, Shen W (2016) Constitutive modeling for flow stress behavior of Nimonic 80a superalloy during hot deformation process. *High Temp Mater Proc* 35:327–336. <https://doi.org/10.1515/htmp-2014-0204>
- [56] Wang M, Li Y, Wen W, Zhou J, Chiba A (2013) Quantitative analysis of work hardening and dynamic softening behavior of low carbon alloy steel based on the flow stress. *Mater Des* 45:384–392. <https://doi.org/10.1016/j.matdes.2012.08.041>
- [57] Kim KW, Park JK (2015) A study of the dynamic recrystallization kinetics of V-microalloyed medium carbon steel. *J Mater Sci* 50(18):6142–6153. <https://doi.org/10.1007/s10853-015-9171-1>
- [58] Cao Y, Di H, Misra RDK, Yi X, Zhang J, Ma T (2014) On the hot deformation behavior of AISI 420 stainless steel based on constitutive analysis and CSL model. *Mater Sci Eng A* 593:111–119. <https://doi.org/10.1016/j.msea.2013.11.030>

Publisher's Note Springer Nature remains neutral with regard to jurisdictional claims in published maps and institutional affiliations.